Electronic Supplementary Materials

For https://doi.org/10.1631/jzus.A2600179

Tunable gated strain sensor integrating detachable metamaterial structures for personalized motion recognition

Ziao SHEN[1,2,3], Minjian WANG[1,2,3], Xiujun FU[1,2,3], Guangqiang ZHANG[1,2,3], Xiangtao PAN[1,2,3], Ye QIU[1,2,3], Yi SONG[1,2,3], Aiping LIU[4], Ye TIAN[1,2,3], Huaping WU[1,2,3]

[1]*College of Mechanical Engineering, Zhejiang University of Technology, Hangzhou 310023, China*
[2]*Zhejiang Key Laboratory of High-Precision and Efficiency Hybrid Processing Technology and Equipment, Zhejiang University of Technology, Hangzhou 310023, China*
[3]*Key Laboratory of Special Purpose Equipment and Advanced Processing Technology, Ministry of Education, Zhejiang University of Technology, Hangzhou 310023, China*
[4]*Center for Optoelectronics Materials and Devices, Zhejiang Sci-Tech University, Hangzhou 310018, China*

Note S1. Performance Regulation Mechanism

To theoretically elucidate the intrinsic correlation between the Poisson's ratio of the substrate material and the closure behavior of micropillar channels, a detailed analysis is presented as follows. The width variation of the conductive liquid channel between wedge-shaped micropillars before and after stretching is depicted in Fig. 2(b). The initial total width of the channel is defined as W, which changes to W' after a longitudinal strain is applied to the sensor. The longitudinal strain is denoted as ε_y, the electrical conductivity of the conductive liquid is denoted as ρ, and the Poisson's ratio of the substrate material is denoted as v.

In the smooth channel devoid of microcolumns, according to the law of resistance：

$$R = \frac{\rho L}{S} \tag{S1}$$

Where R represents the resistance value; L represents the length of the resistor; and S represents the cross-sectional area.

The ratio of the resistance value R' after stretching to the initial resistance value R_0 is：

$$\frac{R'}{R_0} = \frac{W}{W'} \tag{S2}$$

Under the condition of maintaining a constant longitudinal strain, changes in width are solely dependent on the material's Poisson's ratio. This is determined by the Poisson's ratio formula：

$$v = -\frac{\varepsilon_x}{\varepsilon_y} \tag{S3}$$

The width W' of the stretched channel can be expressed as：

$$W' = W\left(1+\varepsilon_x\right) = W\left(1-v\varepsilon_y\right) \tag{S4}$$

Therefore, Equation (2) can be expressed as：

$$\frac{R'}{R_0} = \frac{1}{1-v\varepsilon_y} \tag{S5}$$

In this scenario, the resistance change of a smooth-channel sensor after stretching depends solely on the material's Poisson ratio. With the introduction of micro pillar structures, the flow path of the conductive liquid within the sensor is altered, and its equivalent resistance can be decomposed into two components: R_1 corresponding to the gaps between transversely adjacent micro pillars,

and R_2 corresponding to the gaps between longitudinally adjacent micro pillars. Resistance R_2 primarily represents the continuous liquid channel along the stretching direction between micro pillars; its geometric characteristics and resistance behavior are essentially identical to those of a smooth channel without micro pillars, and thus will not be further discussed. This study focuses on the transverse resistance R_1, which is predominantly governed by micro pillar gap regulation. This component exhibits high sensitivity to variations in micro pillar spacing and is crucial for achieving high sensor sensitivity through the gating effect. The rate of change in resistance between the lateral channels of microchannels can be expressed as：

$$\frac{R_1'}{R_1} = \frac{D}{D'} \tag{S6}$$

Where R_1 represents the initial resistance between the lateral microcolumns; R_1' denotes the resistance value between them after stretching.

The lateral spacing after stretching can be expressed as：

$$L + D' = (1 + \varepsilon_x)(L + D) \tag{S7}$$

Set the proportional relationship between the horizontal micropillars and their spacing as follows：

$$\boldsymbol{L + D = \lambda D} \tag{S8}$$

Substituting into equation (6) yields：

$$\frac{R_1'}{R_1} = \frac{1}{1 - \lambda \nu \varepsilon_y} \tag{S9}$$

Since the λ value is significantly greater than 1, the introduction of micro columns induces substantial resistance changes. When tensile strain causes the lateral spacing between micro columns to gradually decrease and approach zero, the sensor exhibits an extremely high relative resistance change rate—the steepness of this resistance response far exceeds that of a smooth channel structure without micro columns, differing by several orders of magnitude. When D' is set to zero, it indicates that adjacent microcolumns begin to contact horizontally; the corresponding longitudinal strain at this point represents the threshold strain ε_{th} for microcolumn closure：

$$\varepsilon_{th} = \frac{D}{\nu(D + L)} \tag{S10}$$

As shown in Equation (10), when the micro pillar spacing ratio λ is fixed, the sensor's threshold strain is determined solely by the Poisson's ratio ν of the substrate material. This provides a crucial theoretical basis for dynamically controlling sensor performance: by altering the device's Poisson's ratio, the threshold strain can be reversibly adjusted without modifying the micro pillar geometry.

Note S2. Finite Element Simulation Parameters

Finite element analysis was performed using the commercial software Abaqus 2023. The flexible substrate was set to be 20 mm in length, 20 mm in width, and 1 mm in thickness. The square micropillar was a cube with a side length of 1.5 mm. The wedge-shaped micropillar was modified from the square micropillar by connecting the midpoints of three sides on the upper surface to form a pentagonal micropillar. The spacing between micropillars was set to 0.5 mm. The entire assembly was assigned as an incompressible Mooney-Rivlin material with material constants C_{10} = 0.144, C_{01}=0.036 = 0.036, and D_1 = 0.1. The perforated plate unit cell had a density of 970 kg/m³, a Young's modulus of 750 kPa, and a Poisson's ratio of 0.49. The boundary conditions are shown in Fig. S8.

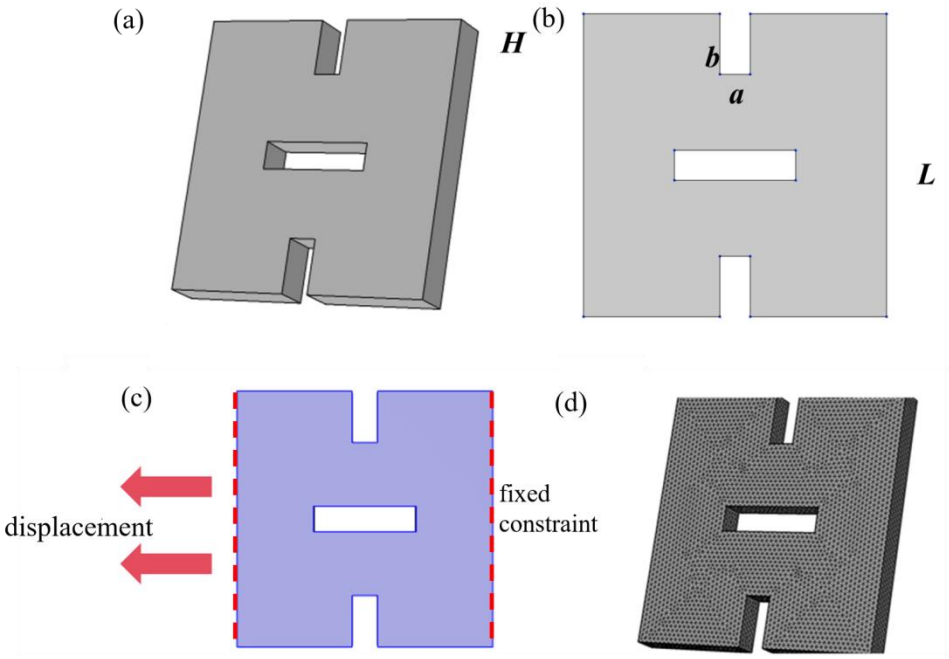


Fig. S1. Perforated plate unit cell structure and simulation parameters: (a) unit cell thickness *H*; (b) unit cell hole width *a*, hole length *b*, and overall size *L*; Numerical simulation conditions: (c) boundary conditions, (d) Grid Settings.

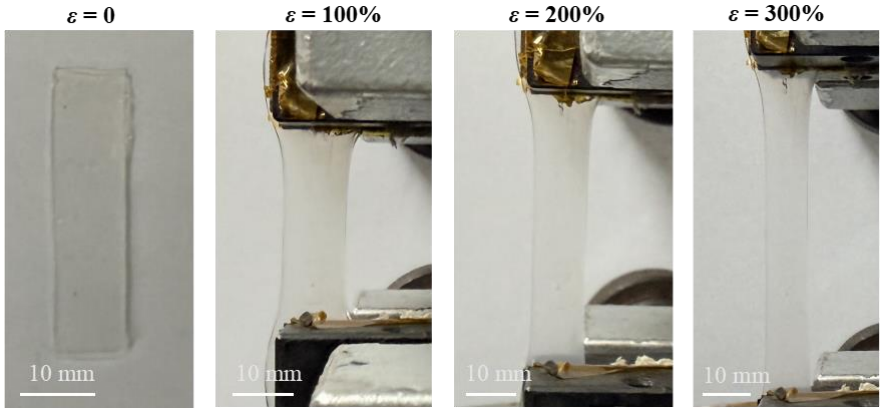


Fig. S2. Photographs of gated strain sensor before and after applying a tensile strain of 100%, 200%, and 300%.

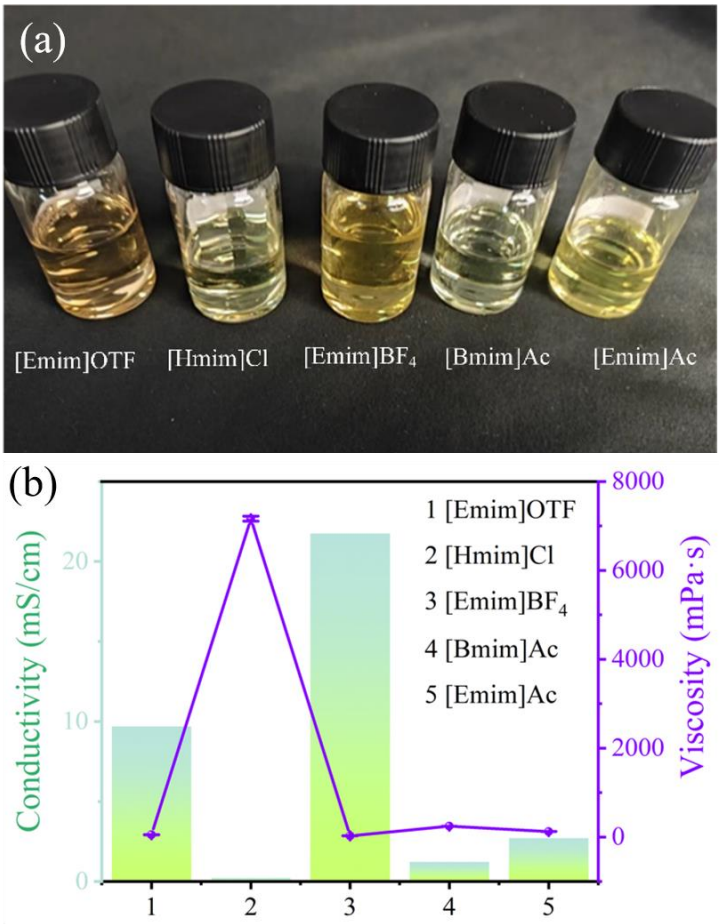


Fig. S3. (a) Five ionic liquid samples; (b)Conductivity and viscosity of five samples at 98% concentration.

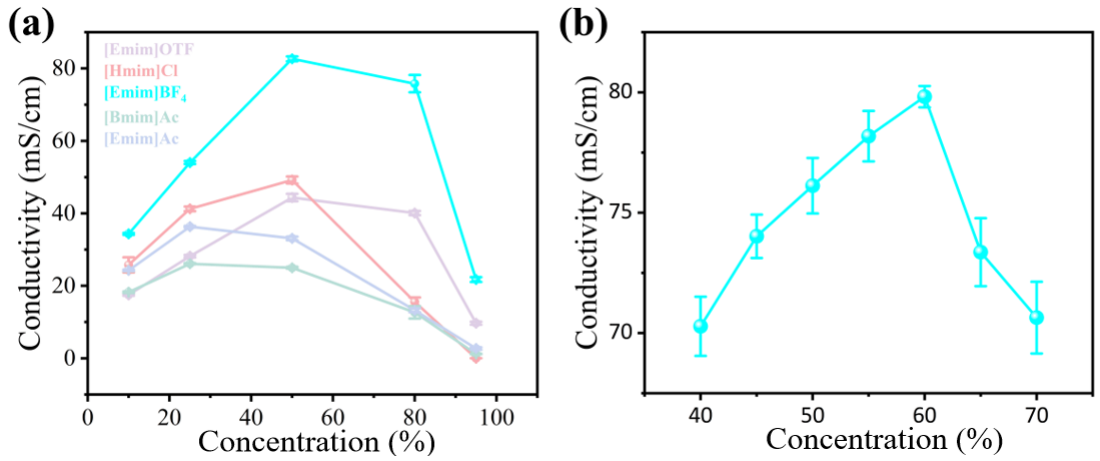


Fig. S4. Conductivity values of liquid materials at different concentrations: (a) Conductivity of five ionic liquids at five concentrations, (b) Conductivity at 40% to 70% concentration of $[Emim]BF_4$.

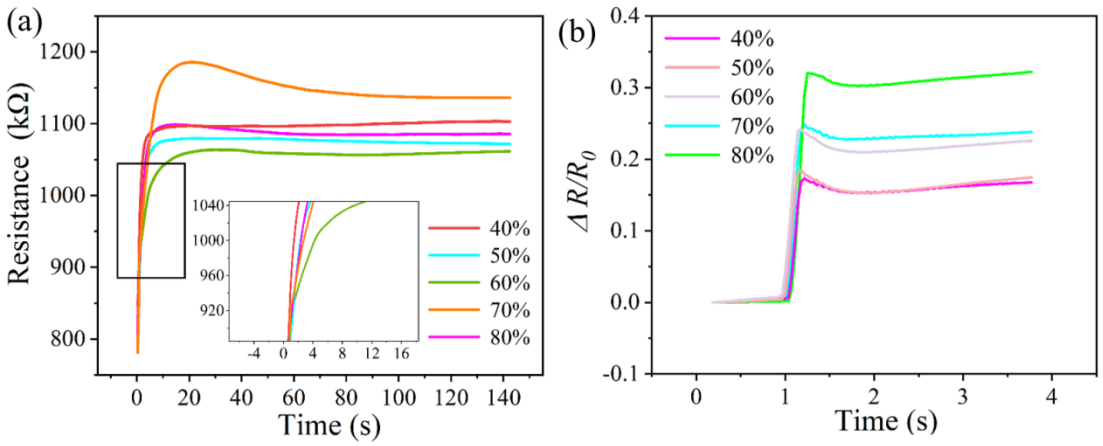


Fig. S5. Effect of [Emim]BF_4 Concentration: (a) The resistance stability value of the sensor at different concentrations of [Emim]BF_4; (b) The resistance change rate of the sensor at different concentrations of [Emim]BF_4 when the tensile strain is 5%.

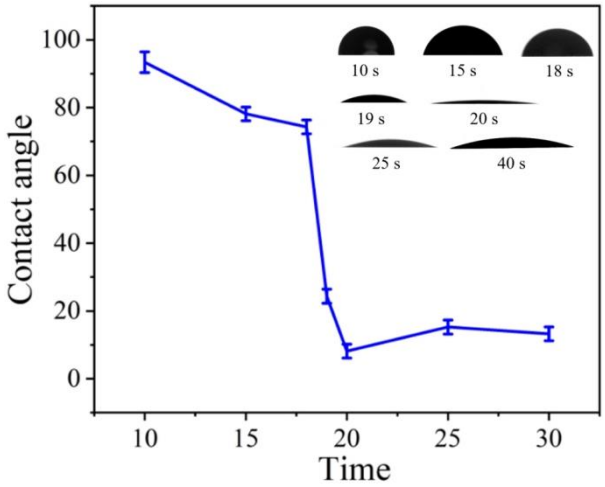


Fig. S6. Side view of droplet and contact angle of substrate under different plasma treatment duration.

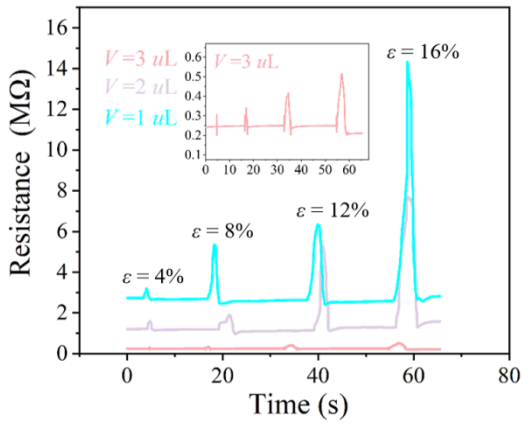


Fig. S7. Tensile response of strain sensor of [Emim]BF_4 in channel under three volumes.

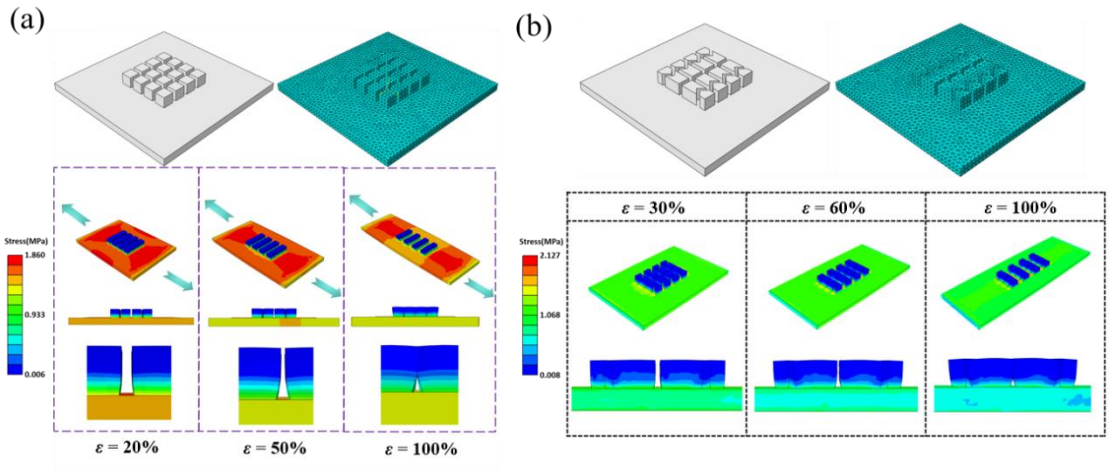


Fig. S8. Gated structure modeling and finite element tensile simulation: (a) square micro-pillar; (b) wedge-shaped micro-pillar.

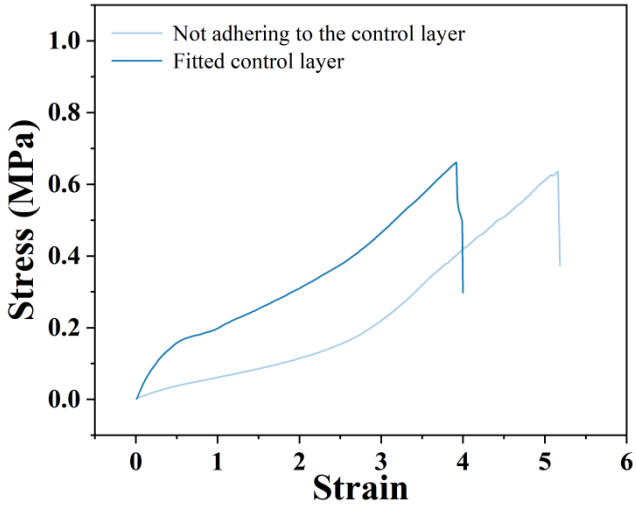


Fig. S9. Tensile stress–strain curve of the gated strain sensor with non-adhering and fitted control layers.

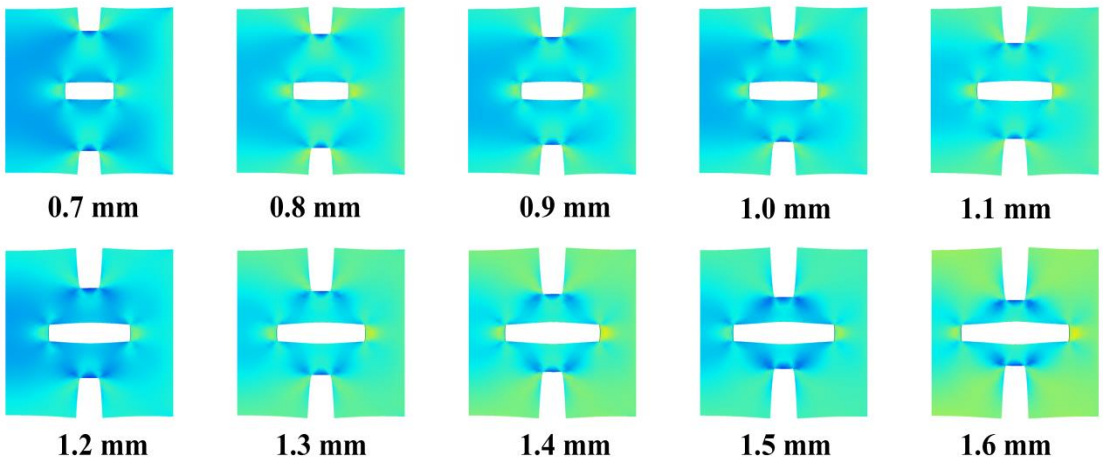


Fig. S10. The deformation of the perforated plate when the cell length *b* increases from 0.7 mm to 1.6 mm.

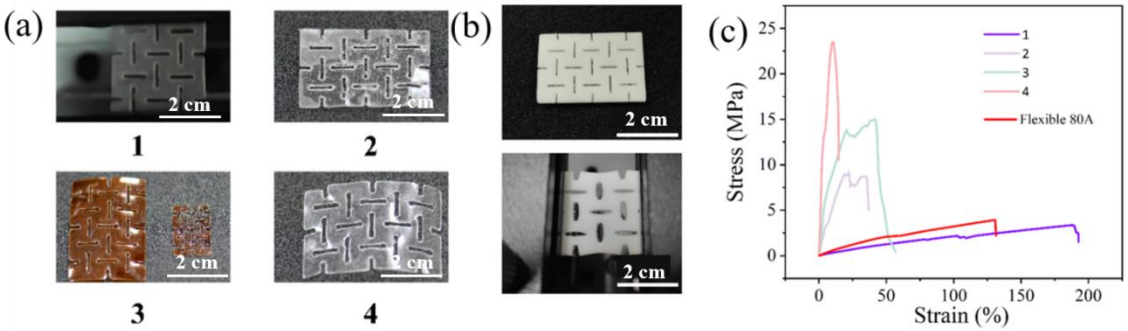


Fig. S11. (a) Laser cutting perforated plate structure: (1) Silica gel. (2) Plastic paper. (3) Polyimides. (4) Polyethylene. (b) The perforated plate structure printed with Flexible resin (Flexible 80A) consumables. (c)Stress-strain curves of five kinds of perforated plate materials.

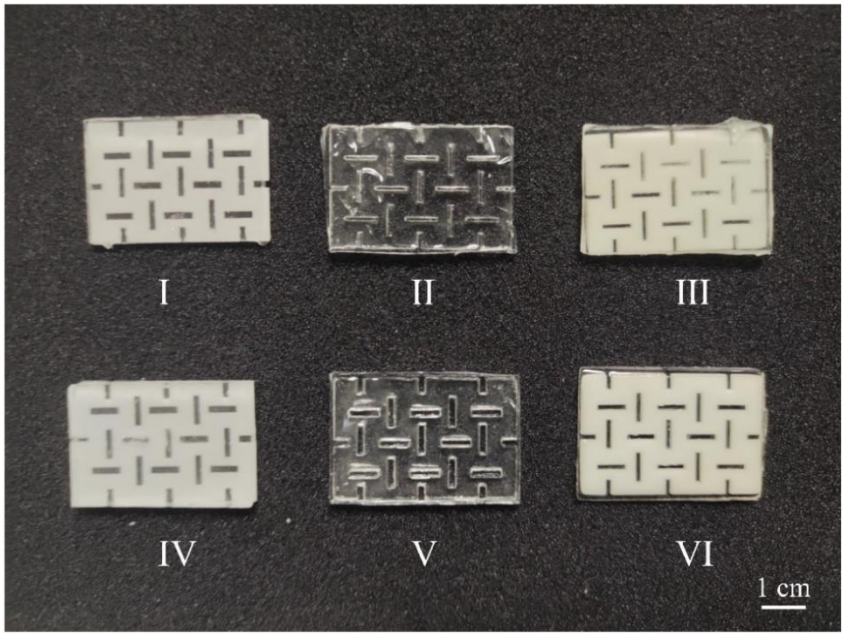


Fig. S12. Part of the perforated plate base patch with different parameters.

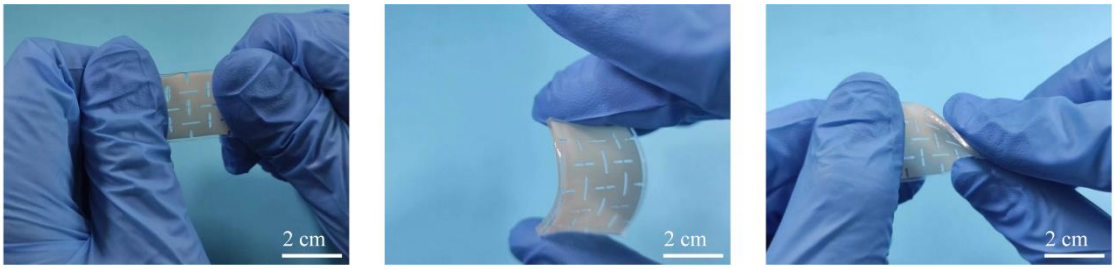


Fig. S13. Stretch, bend and twist PDMS embedded with perforated plate materia.

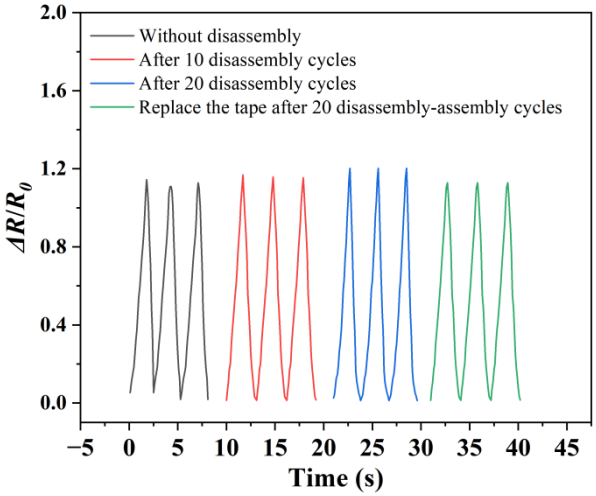


Fig. S14. Real–time responses of the gated strain sensor under 10% strain after different disassembly cycles.

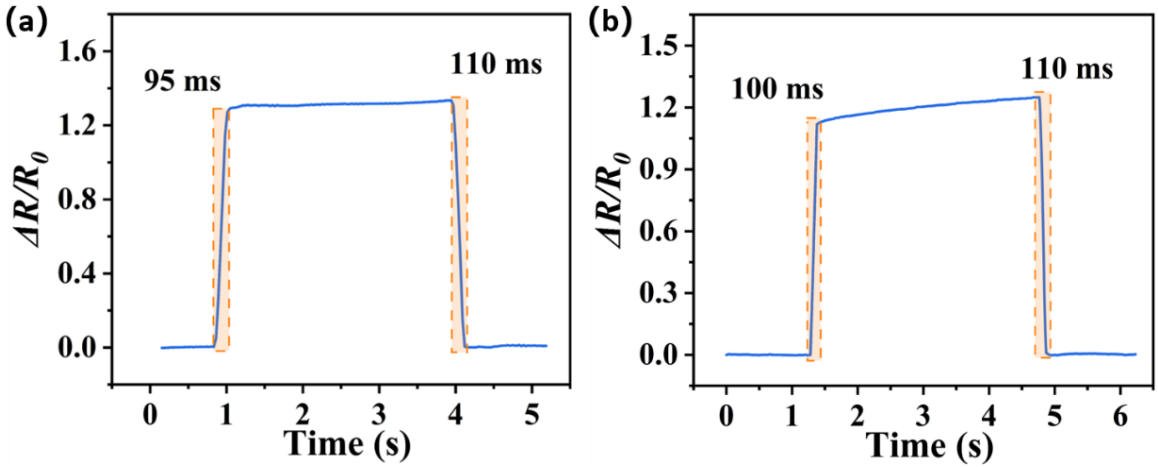


Fig. S15. Response and recovery times of the gated strain sensor under 10% strain. (a) The sensor is not attached to the metamaterial layer. (b) The sensor is attached to single-sided metamaterial layer.

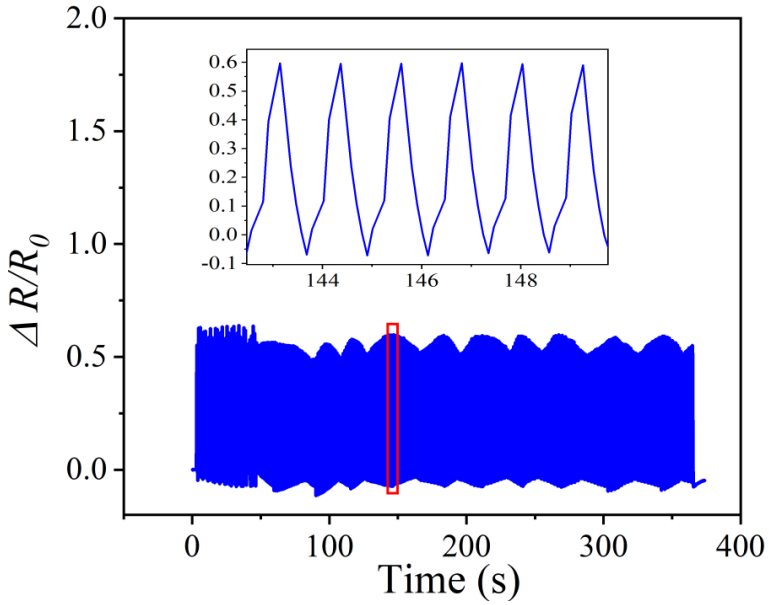


Fig. S16. 200 cyclic tensile tests were carried out under 5% strain after 30 days

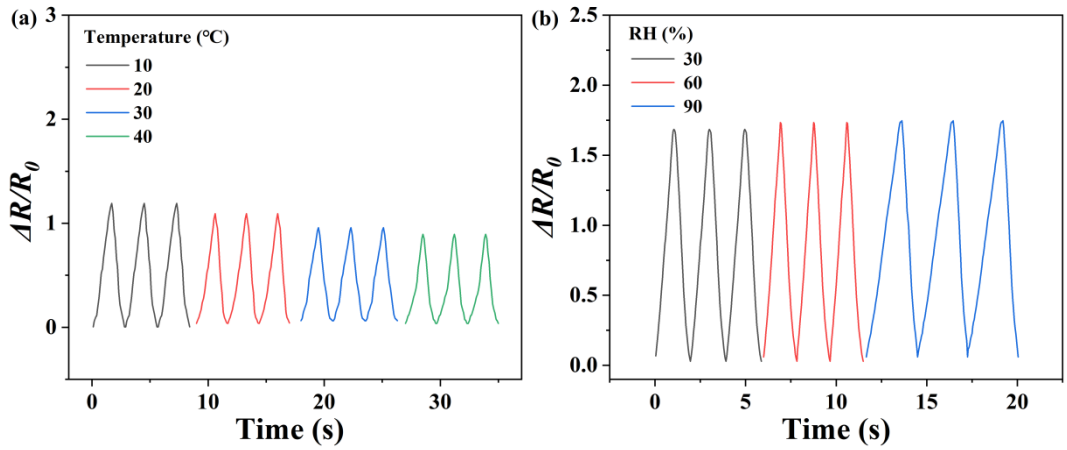


Fig. S17. Real–time responses of the gated strain sensor under 10% strain at different temperatures and humidities. (a) Temperature variation (RH = 30%). (b) Humidity variation (Temperature = 20 °C).

Table S1. Comparison of sensing performance of flexible strain sensors.

Material	Sensing range (%)	Gauge factor	Detection limit (%)	Ref
Agarose/PHEA DN Ionogel	50	0.93	1	Nishikawa et al., 2023
CS-(AA-HEMA-DN) Ionic-gel	100	1.6	1	Sun et al., 2020
Cho-A_x Ionogels	100	2.02	1	Chen et al., 2022
Zwitterionic Lignin-Mediated Hydrogel	150	3.3	1	Fang et al., 2025
PSM/TF/Zn^{2+}	200	5.6	1	Guo WY

Zwitterionic Hydrogel				et al., 2023
LM/PDM	80	1.05	0.2	Guo et al., 2023
PER/EM	100	3.2	0.5	Wan et al., 2019
HEMA-EG Hydrogel/LM	200	1.7	0.5	Yang et al., 2023
LM/PDMS/Cr-Au	10.68	2230	0.05	Jeong et al.,2024
PDMS/Ionic-Liquid	50	45300	0.05	Luo et al., 2023
LM/PDMS/Ecoflex	140	2295	0.04	Luo et al., 2024
Ecoflex /Ionic-Liquid	100	6640	0.05	This work